energies

Article

Design and Realization of an Inductive Power Transfer for Shuttles in Automated Warehouses

Massimo Ceraolo [1], Valentina Consolo [1], Mauro Di Monaco [2], Giovanni Lutzemberger [1], Antonino Musolino [1,*], Rocco Rizzo [1] and Giuseppe Tomasso [2]

[1] Department of Energy, Systems, Territory and Constructions Engineering, University of Pisa, Lungarno Antonio Pacinotti, 43, 56126 Pisa, PI, Italy; massimo.ceraolo@unipi.it (M.C.); valentina.consolo@phd.unipi.it (V.C.); giovanni.lutzemberger@unipi.it (G.L.); rocco.rizzo@unipi.it (R.R.)
[2] Department of Electrical and Information Engineering "Maurizio Scarano", University of Cassino and Southern Lazio, Viale dell'Università, 03043 Cassino, FR, Italy; m.dimonaco@unicas.it (M.D.M.); tomasso@unicas.it (G.T.)
* Correspondence: antonino.musolino@unipi.it; Tel.: +39-050-2217321

Citation: Ceraolo, M.; Consolo, V.; Di Monaco, M.; Lutzemberger, G.; Musolino, A.; Rizzo, R.; Tomasso, G. Design and Realization of an Inductive Power Transfer for Shuttles in Automated Warehouses. *Energies* **2021**, *14*, 5660. https://doi.org/10.3390/en14185660

Academic Editor: Chunhua Liu

Received: 21 July 2021
Accepted: 2 September 2021
Published: 9 September 2021

Abstract: The inductive power transfer (IPT) is expected to greatly contribute towards electrification in transportation. In fact, IPT charging technology has the potential to overcome several limitations of conductive charging: in particular, the process can be fully automatable, and both static and dynamic charging are allowed, thus reducing the size of the battery pack. Additionally, safety is increased due to the absence of safety issues related to loss of cable insulation or to the unwanted interruption of the plug-socket connection. This paper presents, from a systematic approach, the design and realization of a prototype for IPT charging of autonomous shuttles in automated warehouses. First of all, the typical mission profile of the shuttle was properly identified, and a storage system based on power-oriented electrochemical cells was sized. Based on that, the architecture of the IPT system was chosen, both for transmitting and receiving sections. The pads were designed for this purpose, by considering the geometric constraints imposed by the manufacturer, through the utilization of the finite elements method. Finally, the power electronic circuitry was also designed. Numerical simulations of the components, as well as of the complete system, were performed and a prototype was built to widely verify the correspondence of the simulation outputs with the results obtained from an experimental measurements campaign.

Keywords: inductive power transfer (IPT); finite elements method (FEM); contactless charging; autonomous shuttle; Ni–MH batteries

1. Introduction

The trend towards electrification is acquiring ever greater importance and diffusion, even in niche sectors such as automatic warehouses. A common architecture of these warehouses is constituted by small shuttles on dedicated guideways to handle goods and materials on and off shelves. They are fed exclusively by an on-board energy storage, in order to avoid noise and pollutant emissions. The MAG-IA project, which stands for "warehouses with artificial intelligence" [1], involves companies and universities working to identify new smart solutions for warehouses, mainly regarding automation and use of energy saving solutions. Thus, the project leader [2] is searching to improve performance regarding the shuttles by changing the storage system on-board and its charging procedure.

In more detail, Figure 1 shows the schematic structure of the automated warehouse in which two shuttles are present, each one having dedicated direction of motion. The shuttle, indicated as *slave*, moves in the y direction; it is typically located on-board the *master*, leaving it for its round-trip missions. The master shuttle moves in the x direction on rails that are installed on a lifting platforms which enables movements in the z direction. In the existing configuration, the slave shuttle uses one supercapacitor as storage device. Due to its low specific energy, this is only able to guarantee one single round-trip mission at very low speed, with the further requirement of the installation of an additional backup source of energy, e.g., one lithium battery kept at the voltage that can be continuously maintained without any damage. This battery is able to guarantee the return trip in the case of unavoidable supercapacitor full discharging. The supercapacitor pack is normally recharged in a conductive way, through one power supply installed on-board the *master* shuttle, while the additional lithium battery can be periodically charged by connecting it to a dedicated external power supply.

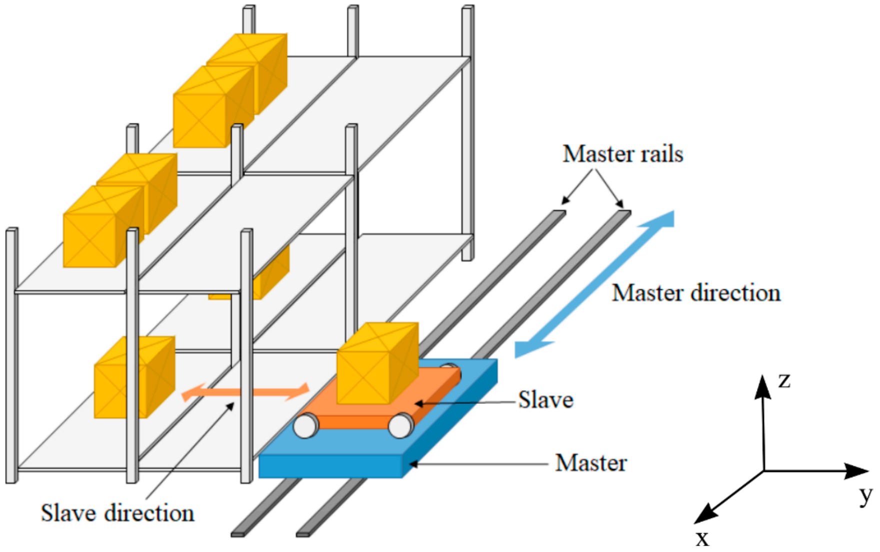

Figure 1. Basic structure of an automated warehouse (courtesy of [3]). The slave moves in y direction while the master is able to move in both x and z directions.

This solution presents several drawbacks. First of all, volume and mass of the whole battery-supercapacitor package can reach considerable values for the installation on-board the shuttle. Hence, investigation for a different monolithic storage solution is of interest, therefore having the same performance in terms of peak power as the supercapacitor, with an additional amount of energy as well, without the need of a backup additional battery. Regarding technology, lithium is very often considered today, but costs remain quite high, and safety constraints require the presence of a battery management system (BMS) able to monitor voltage, current and temperature of the cells, by also including the management of equalization during charging operations. For this reason, alternative technologies like Ni–MH cells, widely used before lithium and reconsidered today, can offer significant performance for the considered application at much more reasonable costs and reliability [4–6].

Finally, conventional conductive charging can have significant drawbacks: first of all, unwanted delays can be present, between stopping of shuttle and beginning of charging; then, due to possible wear of cable insulation and possible formation of electric arcs due to accidental interruptions of the plug-socket connection, conductive charging may show some significant safety issues. On the other hand, inductive charging presents a higher degree of safety, without risk of fire and explosions, and can be fully and easily automated [7,8]. The only drawback is due to the maximum available charging power, often limited in the range of 3–5 kW. However, although in automotive applications this can be classified as slow charging power, for the system under consideration it is more than adequate to guarantee full charging of the slave shuttle, in the order of a few seconds.

Inductive power transfer has been long applied for the charging of electrical vehicles and for implementing bidirectional energy flows [9,10]. Current literature reports several applications, most of them focused on the components of the IPT system. In particular, some authors [11,12] report exhaustive reviews of the state of the art of the wireless power transfer (WPT) under a circuital point of view without considering neither the design of the pads, nor the driving power electronics. Other authors [13] only consider the power electronic aspects related to IPT, while the simple circuital model based on coupled inductors is adopted for the pads. Authors in [14–16] consider the transfer of small powers while investigating the aspects of data transfer through the coupled pads. On the other hand, authors in [17] discuss an IPT system for low power levels focusing on the power electronics and its control algorithm, while considering two simple circular coils as transmitting and receiving pads. An interesting approach to the optimization of an underwater IPT system, also considering the eddy current losses in the medium surrounding the pads, is discussed in [18]. The semi-dynamic IPT for autonomous vehicles at power levels up to 11 kW is described in [19].

From this short review we see that most of the current literature lacks a "system" approach, since it covers just a few detailed aspects, without the presence of a full-integrated design approach, which in this paper moves from the mission profile definition, storage sizing, design of pads and power electronics, up to the realization of the final prototype.

In particular the authors of this paper describe a full design of an IPT system where several constraints deriving from a pre-existent mechanical layout are imposed (i.e., position and extension of the pads on master and slave shuttles). This requires an "ad hoc" sizing of the pads and a subsequent integration with the power electronics which is designed on purpose considering the required transmitted power and the prescribed levels of the voltages from the power grid on the master shuttle and on the battery pack on board of the slave. The description of this coordinated design represents the added value of this paper.

The paper is structured as follows. After briefly showing the working cycle under consideration and the sizing of the newly installed storage system, attention is firstly focused on the design of the transmitting and receiving pads and on their equivalent lumped circuit parameters. Subsequently, the compensating networks are chosen according to the considered application, then the dedicated power electronics is designed. Finally, the results obtained by numerical simulations are compared with the measured data taken on a full-scale prototype.

2. Sizing of the Storage System

Following the considerations made in the introduction and regarding the replacement of the energy storage system on the shuttle, the project leader [2], after investigating the market, selected a battery pack composed by Ni–MH high power cells [20]. The authors already tested the proposed Ni–MH cells [3], and concluded that, for the considered power solicitations, this technology is fit for the purpose, and competitive with the most common lithium-based solutions.

In particular, the Ni–MH cell was tested inside a realistic working cycle, representing the real solicitations to which the *slave* shuttle is subjected, during standard working operations. Specifically, a simulation model was realized in Modelica language [21], by following exactly the approach used by the authors in [22–24]. The *slave* shuttle was modeled through a dynamic model, where closed-loop controls have to follow a determined speed cycle, by regulating the electric torque propulsion.

Therefore, typical working operations can be represented, and the energy and power fluxes on the powertrain can be obtained. The implemented working cycle is represented in Figure 2, directly taken from [3] and shown here for clarity.

From the top, the reference and the actual speeds are shown, then the electric drive input power (middle), and finally, the voltage and current from the originally installed on-board storage system, e.g., the supercapacitor stack (bottom). The whole duration is about 50 s, which is the typical duration of loading and unloading operations made from the shuttle in the warehouse, and the maximum peak power is about 1 kW. Next is the charging phase, where the supercapacitor stack reaches 3 kW-power; it takes about 5 s to fully reintroduce the energy spent during the previous working operations.

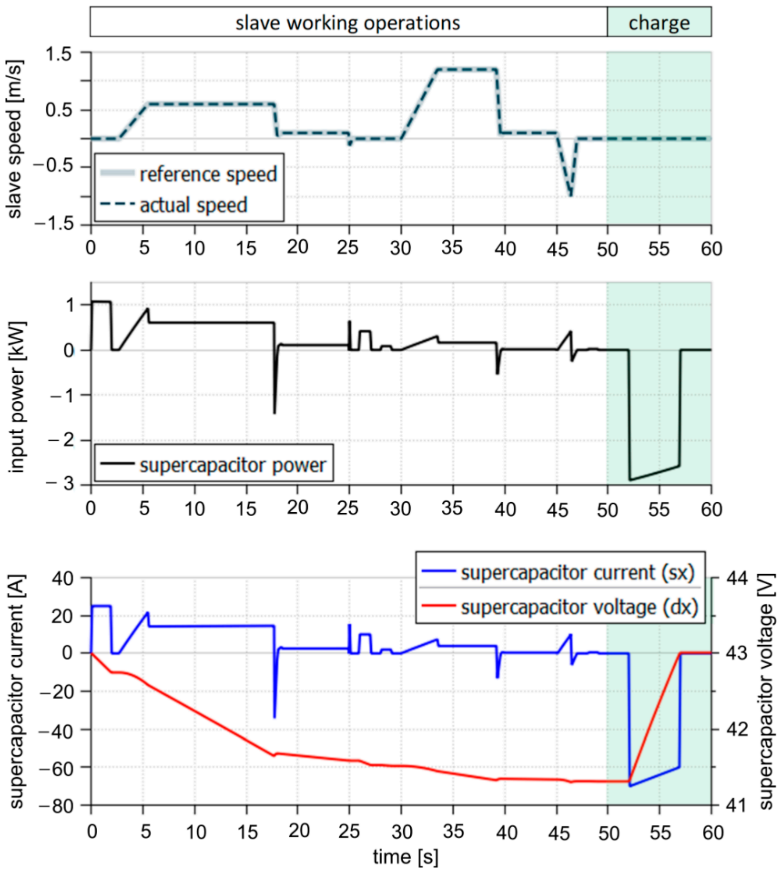

Figure 2. Working profile for the slave shuttle in the original configuration with the supercapacitor. Speed (**top**), electric drive input power (**middle**), storage voltage and current (**bottom**) (courtesy of [3]).

From this working profile, a storage system based on Ni–MH cells was sized. Based on the power needs, and taking the voltage in the same range as the supercapacitor stack, the number of cells in series was chosen. Other characteristics are given in the next Table 1. According to the main goals of the project, it is of interest to remember that, compared to the original supercapacitor stack, reduction in mass and volume was of about 60% and 90%, respectively [3]. On the other hand, the nominal energy significantly rises up, which guarantees an energy reservoir and reduced state-of-charge (SOC) oscillations. This fact influences battery aging, since the number of charging-discharging cycles rises when SOC variation is within a narrow band. More in detail, if the SOC variation is within 5%, the number of the allowed charging-discharging cycles can reach approximatively the hundreds of thousands [25,26], nearly the same as what is expected from supercapacitors [27].

Table 1. Battery pack.

Chemistry	Ni–MH
Nominal capacity (Ah)	6
Nominal voltage (V)	36
Operating voltage (V)	49.5; 24.0
Nominal energy (Wh)	216
Mass (kg)	5.8
Volume (L)	1.9
ΔSOC/cycle (%)	5

3. The IPT-Based Battery Charger

The analysis performed so far allowed the sizing of a storage system on board of the slave based on Ni–MH high power cells. The experimental activity described in [3] confirmed that Ni–MH is able to sustain high power solicitations comparable to those of lithium power-oriented or supercapacitor-based solutions.

Ni–MH technology is confirmed as a valid alternative to lithium iron phosphate (LFP)-based batteries; it is also characterized by an improved stability with fewer safety issues when it has to be used in presence of potentially explosive or inflammable atmosphere or it has to be transferred, e.g., by cargo planes.

The standard working cycle is composed of a 50 s mission (that represents the time typically needed for loading and unloading the slave and its trip in the warehouse) and a charging phase when the battery pack is charged to recover the energy spent during the previous working operation. Charging typically takes no more than 10 s (usually 5 s, ref. Figure 2). The maximum discharge power during the operation is about 1 kW, while the charging power may reach the peak value of about 3.5 kW.

In the original configuration, when the slave is positioned on the master, a plug is connected to the inlet and electrical power from the master flows to the battery, thus realizing a "conductive power transfer".

The following steps can be recognized when the conductive power transfer is adopted:

(a) Park the slave on the master;
(b) Connect the plug to the inlet;
(c) Check for the electrical continuity;
(d) Transfer power to the battery on the slave;
(e) Check for the zero current on the link;
(f) Disconnect the plug.

The above-described sequence is necessary if electric arcs have to be avoided in order to preserve the integrity of the electronic circuits. Considering that the first three steps and the last two may require times in the order of seconds, they can have a significant impact on the overall charging time.

Obviously, accidental disconnections of the plug from the inlet, maybe caused by shocks on the master, cannot be prevented. These events may start fires or explosions in hazardous environments.

An alternative to the conductive power transfer is the inductive power transfer (IPT) that is characterized by several advantages which makes this solution very attractive in the described context. In fact, because of the absence of plugs, IPT is intrinsically free from electric arcs; moreover, the charging can start as soon as the slave has stopped, or even when it is approaching, since power transfer also takes place with partially facing pads [28]. IPT has the unique feature of allowing the dynamic charging, i.e., the charging of batteries while the vehicle is in motion. Dynamic charging would increase driving range while reducing the size of the battery pack and improving its management and life cycle since the battery can be kept in a narrow 40–60% SOC [29].

The block diagram of a typical IPT system for the unidirectional charging of an electric vehicle (EV) is shown in Figure 3.

The three-phase voltage (400 V, 50 Hz) is available on the master shuttle. It is rectified by a three-phase, six-pulse diode bridge; a DC/DC converter may be necessary between the rectifier and the H-bridge inverter used to obtain an AC output which feeds the transmitting side via a compensating network.

The fundamental frequency of the voltage produced by the inverter was chosen at 85 kHz, a value that is becoming standard because of its widespread use.

The system, constituted of the transmitting and receiving pads, is a loosely coupled transformer because of the large separation between the primary and secondary windings. Due to this large windings separation, it has a relatively large leakage inductance; consequently, the power factor is also very poor considering the high operating frequency.

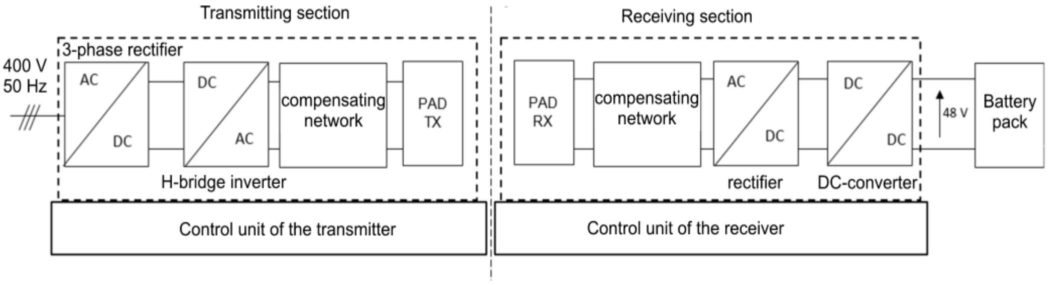

Figure 3. Block diagram of the IPT system. A communication link between the control units allows to control the transferred power.

When the coils of an IPT system operate at a frequency well below their self-resonant frequencies (often in the order of MHz), compensating networks on both primary and secondary sides are introduced to reduce the voltampere rating of the inverter. These compensating networks are substantially constituted by capacitors (also with additional inductors) providing the resonant tanks in both the primary and secondary sides [30,31].

Compensating networks are able to (1) maximize power transfer capability, (2) realize constant-current (or load-independent) or constant-voltage output without a control circuit, (3) achieve high efficiency.

Once the electric power is delivered to the secondary circuit at the working (resonant) frequency of the compensating network, a rectification is performed by a full wave rectifier, and a DC/DC converter is used to adjust the voltage values to the one of the battery pack.

From the above discussion related to the mission profile, the IPT has to be able to deliver a power of about 3.5 kW. This power can be obtained by different values of voltage and current. In order to minimize the currents, high voltages can be chosen, but voltage values that are too high have obvious drawbacks in terms of stress on the insulating materials. On the other side, high currents may impact the design of the output stages of the inverter. For this reason, the designs of the power electronics, of the transmitter and receiver pads, and of the compensation networks are tightly coupled.

In order to realize a constant voltage charging of the batteries, a primary LCL—secondary LC compensating networks were chosen. To maintain a limited current on the secondary, a step-down DC/DC converter (the voltage ratio is approximatively equal to 2) was inserted between the rectifier and the battery. The peak value of the current on the secondary pad is estimated at about 56 A.

This allowed to choose the section of the litz wire used to build the windings of the pads. In particular, we considered a wire with circular cross section with a diameter of 6.5 mm constituted by 2500 wires with diameter 0.1 mm (0.1 × 2500 U-155 G1 2 Mylar, manufacturer Elettrofili [32]).

4. Transmitting and Receiving Pad Design

This section is devoted to the design and the characterization of the transmitting and receiving pads. As usual in IPT systems, the two pads are assumed to be equal and for an optimal operation they should face each other [28,33].

The replacement of the original energy storage system freed up a large amount of space on the slave which allowed to house the receiving pad and the secondary power electronics units, while finding space on the master was not a problem. Considering that the device has to be installed on preexisting mechanical layouts of master and slave shuttles, the available room for both was $\Delta x = 350$ mm, $\Delta y = 210$ mm and $\Delta z = 35$ mm (approximately the size of a 15 inch laptop), while the mechanical clearance between the master and the slave is 50 mm. The main difficulty was to find two corresponding areas one on the bottom of the slave, the other on the top of the master.

Due to the need to insure a protection of the wires that constitutes the windings and that represent the most extern and consequently the more exposed part of the pads, a coating of 5 mm of plastic material is added. The overall distance between the active parts of the pads (i.e., the windings) is then $\Delta h = 60$ mm.

The typology of the pads adopted in the described system is fully reported in [34] and is known as DD pad. The complete geometry is shown in Figure 4 which also reports the main dimensions. In particular, Figure 4a) shows the magnetic cores of the two pads. Each core is constituted by six blocks of N87 MnZn ferrite (the size of the block is 93 mm × 28 mm × 16 mm [35]), arranged in three lines separated by a gap of 5 mm. The two D coils and their relative positions with respect to the ferrite cores are shown in Figure 4b). The coils are wound by a single layer—10 turns of the litz wire before described. Finally, Figure 4c) shows the pads with their 3 mm thick aluminum cases which act as electromagnetic shields. As reported in [34], the distribution of the turns in the center zone of the pad is one of the key parameters of the device, affecting the magnetic coupling k between primary and secondary windings and the uncompensated power. Because of the constraints on the available room, the wire section and the number of turns in the proposed design, the turns in the central zone provide a coverage of about 70% of the length of the magnetic core.

The number of turns and the size and arrangement of the magnetic core were chosen after an iterative design. In correspondence of a candidate pad the corresponding power electronics is designed and the overall cost and performance of the complete system are evaluated. As a result of this test and try analysis, we observed how the transmitting and receiving pads characterized by the values of $L_t = L_r = 50$ µH and $M = 20$ µH at distance $\Delta h = 60$ mm, were good candidates. We performed several numerical analyses carried out by using both an integral formulation developed at DESTEC [36,37] and a commercial FEM code [38]. The integral formulation, because of its ability to provide sufficiently accurate results with coarse discretization and short computation times, was used to identify candidate solutions, while FEM was used to perform more accurate analyses. An innovative approach based on deep neural networks was used to support the last steps of the electromagnetic design [39].

The DC resistance of the windings is about $R_{DC} = 15$ mΩ. When considering the AC resistance at the operating frequency ($f_0 = 85$ kHz) we have to consider the additional losses due to skin and proximity effects on the conductors, the losses in the magnetic core and the losses due to the eddy currents in the shields. The use of litz wire results in low additional losses in the windings; the other losses were estimated by the FEM analysis.

We started considering a linear model of the ferrite obtained by evaluating the initial relative permeability of 2200 at 25 °C, as reported in the manufacturer data sheets [35], while eddy currents are neglected. For the first simulations we assumed a sinusoidal current of 40 A (rms) at the frequency f_0 on one of the pads, while the other, located at the nominal distance $\Delta h = 60$ mm, is open circuited. The expected peak value of the secondary current, estimated at about 56 A is well below the one corresponding to the sinusoidal waveform at 40 A (rms). The hypothesis of linear behavior will be checked again at the end of the design of the power electronic circuitry when the current on the transmitting pad will be known. The resistivity of the aluminum shields was taken as $\rho_{Al} = 2.7 \cdot 10^{-8}$ Ωm.

Figure 5 shows the magnetic flux distribution inside the ferrite cores. Looking at the color scale on the right of the figure we can observe how the maximum values of the flux density modulus is $B_{max} \simeq 100$ mT, which is well below the knee of the magnetization curves as shown on the data sheet. Considering the shape of the magnetization curves at 25 °C provided by the manufacturer, we see that linearity can be assumed up to the flux density $B_{knee} \simeq 300$ mT corresponding to an excitation current greater than 120 A (rms).

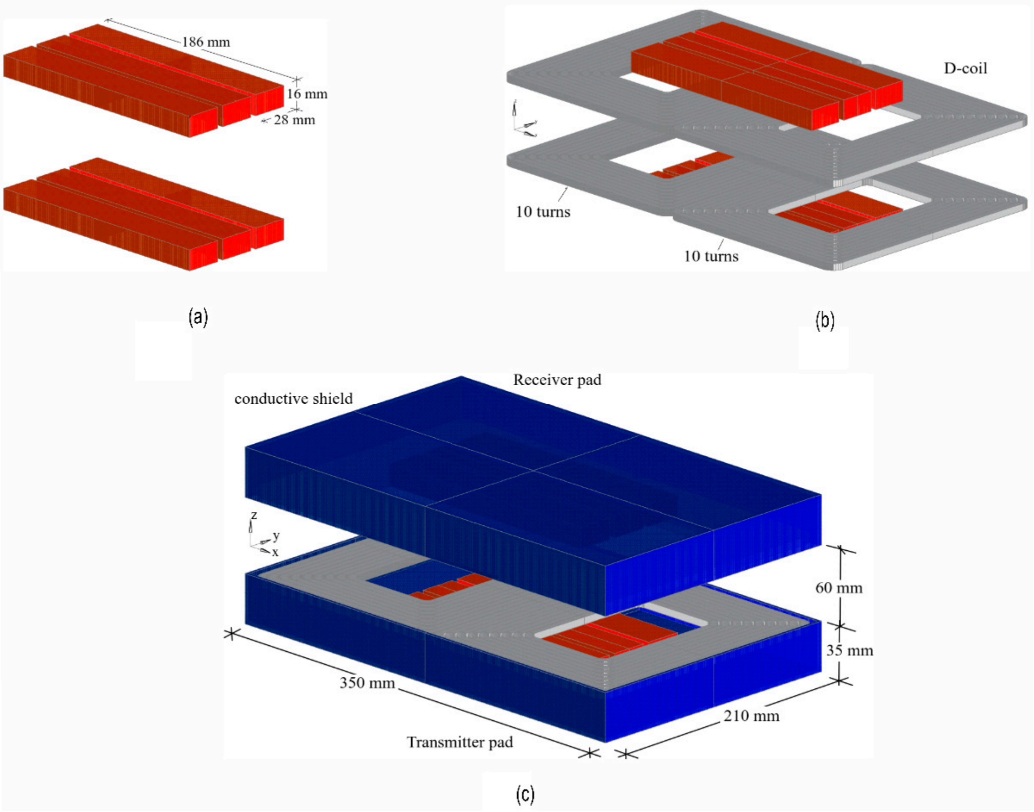

Figure 4. Full 3D views of the transmitter and receiver pads. (**a**) Dimensions and arrangement of the blocks used to build the two cores (6 blocks per core, 12 blocks in all); (**b**) winding (in gray) are added to the cores; (**c**) aluminum shields (in blue) enclose the cores and the windings.

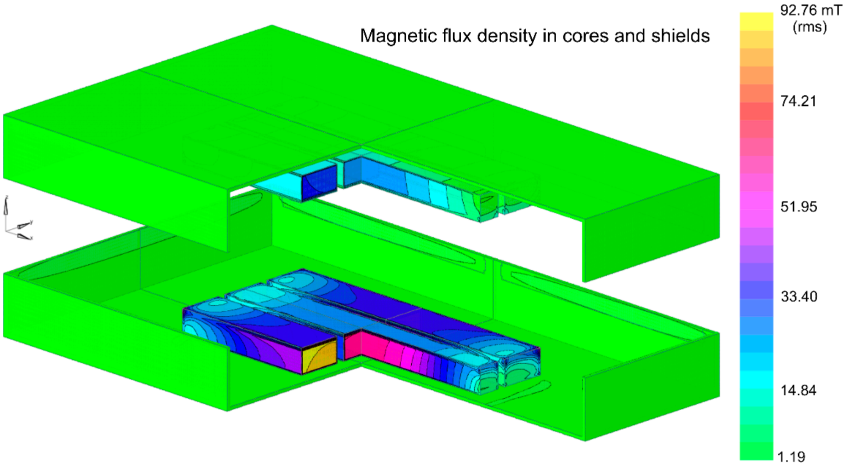

Figure 5. Magnetic flux density distribution in the ferrite cores and in the shields when only the lower winding is fed. The maxima occur in the central section of the outer lines of the ferrite core.

Figure 6 shows the eddy current distribution on the shields. We see that the eddy currents are negligible in the shield of the open circuited winding, while they can assume relatively high values in small regions of the shield of the fed winding. Considering that the most intense currents are localized in relatively narrow regions and that the device is intended for discontinuous operation, the temperature raise is expected to be limited to a few degrees.

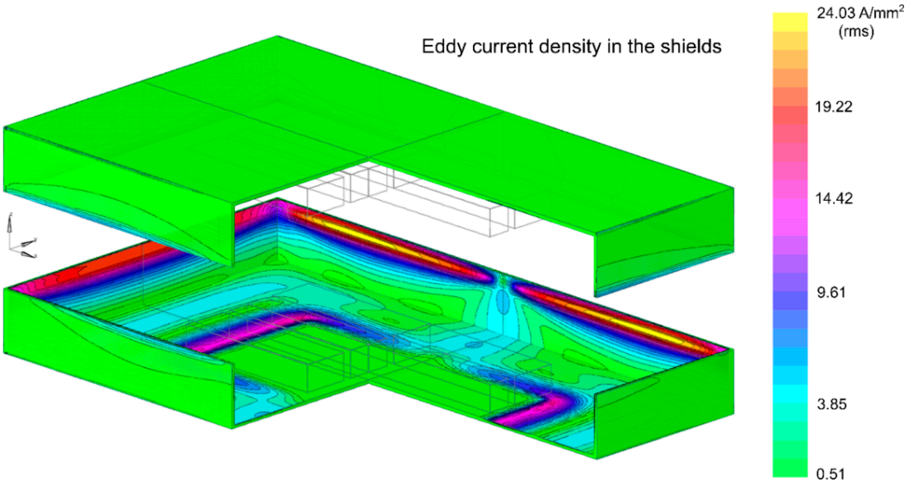

Figure 6. Eddy current density distribution in the shields when only the lower winding is fed. The maxima occur near the edge of the longer sides of the shield. Eddy currents (as well as all the other causes of losses in the ferrite) are neglected.

Once the eddy current distribution J_{Al} in the shields is known, the related losses are evaluated by integration of the loss density $\rho_{Al} J_{Al}^2$ on the volumes occupied by the shields [38]. These losses sum up to $P_{eddy} = 147$ W and are mainly concentrated on the fed pad. The core losses are estimated by a post processing. Preliminarily, the core losses density versus the AC field flux density at the operating frequency f_0 is determined by proper interpolation of the measurement performed by the manufacturer and reported in the data sheets [35]. Data taken from curves reporting the core losses versus frequency at 25, 50, 100 and 200 mT (rms) were used to obtain four points of the curve expressing the core losses at f_0 versus the AC magnetic flux density. The curve so obtained is reported in Figure 7.

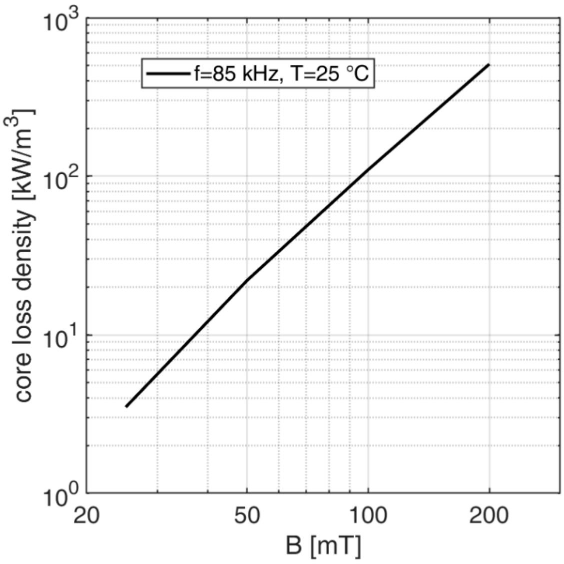

Figure 7. Losses in the ferrite core vs. AC magnetic flux density at 85 kHz and 25 °C. This curve is obtained by interpolation of the manufacturer data sheets reported in [35].

By using this curve and the flux density distribution in the core the power losses density is obtained and the total losses are evaluated by integration. Computed losses in core are $P_{core} = 35$ W. Total losses are $P_1 = P_{core} + P_{eddy} = 182$ W.

The computed values of self-inductance of a pad obtained with a fine mesh and when the other pad is open-circuited are: $L_t = L_r = 49.3$ µH, $X_t = X_r = 26.3\ \Omega$ (at $f_0 = 85$ kHz).

The voltage corresponding to the feeding current of 40 A (rms) at the given frequency is $E_1 \cong 2\pi f L_t I_1 = X_t I_1 = 1050$ V (rms). Considering that the core and the eddy current losses on the shield are related to the square of the feeding voltages, we can build the "classical" equivalent circuit as shown in Figure 8a.

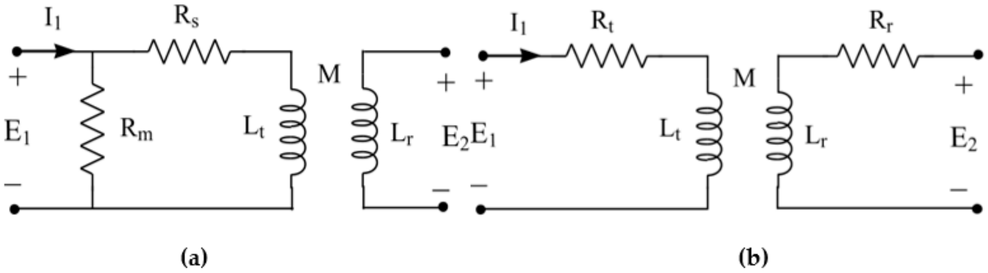

Figure 8. Equivalent circuits of the coupled pads. (**a**) transformer-like "classical" equivalent circuit; (**b**) specific equivalent circuit.

We can assume for R_s its DC value: $R_s = 15$ mΩ, while $R_m = E_1^2/P_1 = 6.06$ kΩ. Considering that $R_m \gg \sqrt{R_s^2 + X_t^2}$, we can discard the fraction of current on R_m, assuming that the whole current I_1 flows on L_t. Under this hypothesis we can use the simpler equivalent circuit as in Figure 8b. In this circuit $L_t = L_r$ and M remain unchanged while $R_t = 0.13\ \Omega$ ($R_t I_1^2 \cong R_s I_1^2 + E_1^2/R_m = 206$ W).

Considering that the core losses (in the ferrite blocks) and eddy current losses (in the shields) are mostly concentrated on the fed pad, while they are almost negligible on the other, we can assume that they are related to the leakage fluxes and not to the common flux as usually happens in ordinary transformers. This means that when the receiving pad is also fed, we just need to introduce the resistance $R_r = R_t$ series connected to L_r , to take into account the additional losses introduced by the secondary current.

5. Power Electronics Design

This section will discuss the sizing of the power electronics circuitry and of the compensating networks on the basis of the expected values of voltage and currents in the system. Once the voltage and the power levels on the load (the battery) are assigned and the characteristics of the transmitting and receiving pads (and consequently the equivalent circuit) are obtained, we can start the design of the compensating networks and of the power electronics [40].

As already anticipated, in order to achieve a constant voltage charge of the battery, a primary LCL and a secondary LC compensation were chosen.

According to this choice, and considering the equivalent circuit of the coupled pads, we obtain the following electrical scheme reported in Figure 9. The symbols used in the equations of this section are shown in the same figure and contextually defined.

In the remaining of the manuscript the following notations are adopted: uppercase letters are used for DC quantities or for real parameters; lowercase letters are used for time varying quantities (e.g., v_i), lowercase letters with hat are used for peak values (e.g., $\hat{i}_r$); uppercase letter with point for phasors (e.g., $\dot{I}_t$), uppercase letters with segment for complex impedance (e.g., $\overline{Z}_p$).

In order to limit the current on the secondary pad as well as on the rectifier, a step-down DC/DC converter was inserted between the rectifier and the load. Considering that the voltage at the battery terminals is $V_{bat} = 48$ V, and that the output voltage of the rectifier is $V_{DC} = 100$ V, the DC/DC converter implements a conversion ratio $V_{DC}/V_{bat} \simeq 2$. Assuming for the efficiency of the DC/DC converter the value $\eta_{DC;DC} = 0.98$, to obtain an output power of $P_{bat} = 3.5$ kW, the input power $P_{DC} = P_{bat}/\eta_{DC;DC} = 3.57$ kW is required.

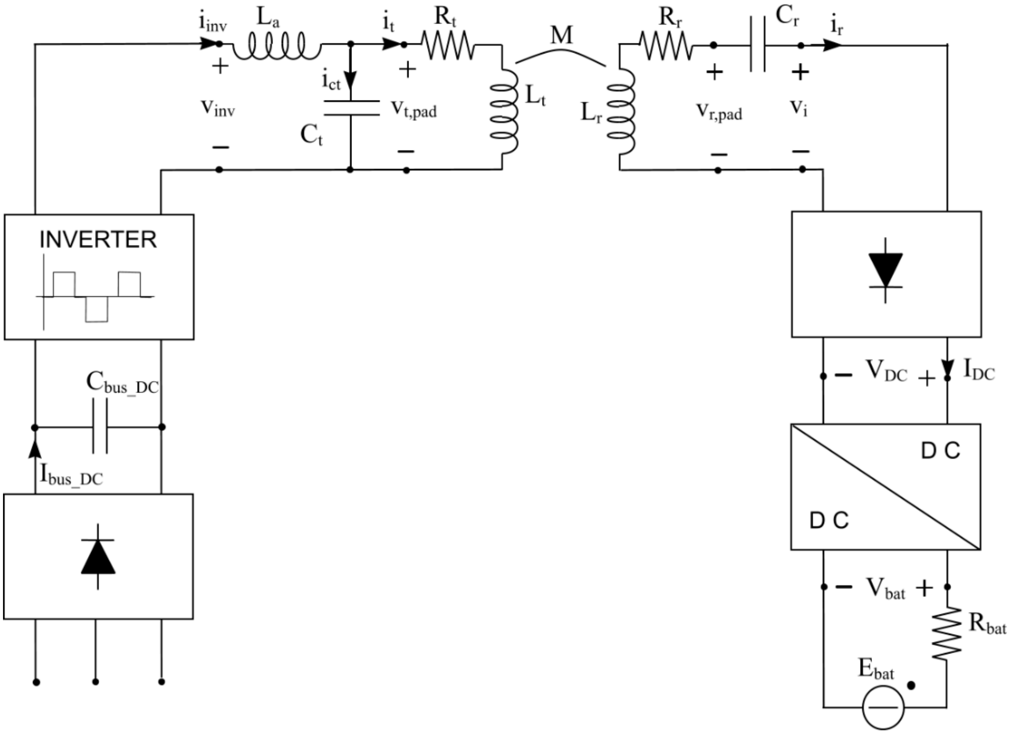

Figure 9. Electrical scheme of the IPT kit: equivalent circuits of the pads and of the compensating networks (LCL type on transmitter and LC series on receiver) are considered. The battery pack is modeled as a series connection between a resistance R_{bat} and a constant voltage source V_{bat}.

Figure 10 shows the equivalent circuit of the receiving section where the DC/DC converter with the load at its output terminals is represented as a resistive load characterized by the absorbed power P_{DC} at the voltage V_{DC}: $R_L = V_{DC}^2/P_{DC} = 2.8\ \Omega$. A capacitive filter based on the capacitor C_{in} is introduced to reduce the ripple of the rectified voltage.

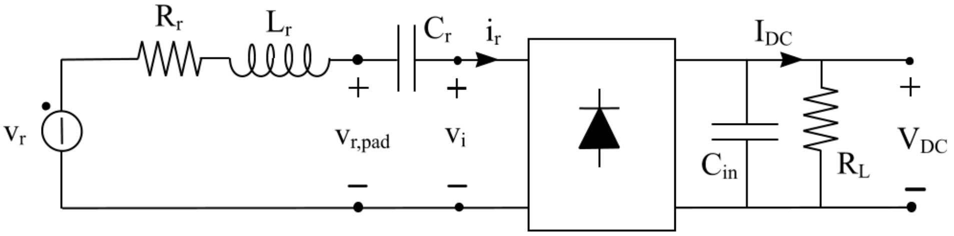

Figure 10. Equivalent circuit of the receiving section: the DC/DC step-down converter and the battery pack are modeled as a resistive load R_L with a rated power of 3.57 kW.

The corresponding current on R_L is:

$$I_{DC} = \frac{P_{DC}}{V_{DC}} = 35.7 \text{ A} \tag{1}$$

The peak value of the input current to the rectifier (approximated by its fundamental) is then (Figure 10):

$$\hat{i}_r = \frac{\pi}{2} I_{DC} = 56.1 \text{ A} \tag{2}$$

Because of the presence of the series resonant compensation network, the voltage at the input terminal of the rectifier ($\hat{v}_i$) can be assumed as a square wave whose peak values are obtained by summing the forward bias voltage ($V_\gamma = 2$ V) of the diodes to the output (constant) value:

$$\hat{v}_i = V_{DC} + 2V_\gamma = 104 \text{ V} \tag{3}$$

In series resonant conditions, the fundamental of the current i_r is in phase with the fundamental of the voltage v_i, and as a consequence the fundamental of the voltage drop on the resistance is in phase with v_i; the peak value of the fundamental of the induced voltage on the receiving pad is:

$$\hat{v}_r = R_r \hat{i}_r + \frac{4}{\pi}\hat{v}_i = 137.5 \text{ V} \tag{4}$$

obtained as the sums of the fundamental components of v_i and of the fundamental of the voltage drop on the secondary winding resistance (Figure 10). $\hat{v}_r$ is the component of the voltage on the receiving pad due to the current in the transmitting pad only. Because of the LC series resonance, the resultant of the fundamental components of the voltages on C_r and L_r due to the current $\hat{i}_r$ is zero.

The value of the series resonant capacitor C_r is:

$$C_r = \frac{1}{\omega^2 L_r} = 70 \text{ nF} \tag{5}$$

The voltage on C_r is:

$$\hat{v}_{C_r} = \frac{\hat{i}_r}{\omega C_r} = 1497 \text{ V} \tag{6}$$

To properly choose the capacitor, we have to consider that its current has a peak value $\hat{i}_r = 56.1$ A. These values of voltage and current indicate the need to use a capacitor bank.

At the resonance frequency, the receiving section can be considered as a resistive impedance obtained as the ratio between $\hat{v}_r$ and $\hat{i}_r$:

$$\overline{Z}_p = R_p = \frac{\hat{v}_r}{\hat{i}_r} = 2.45 \ \Omega \tag{7}$$

The peak value of the fundamental of the resultant voltage at the terminal of the receiving pad (including the terms of self and mutual induction, as well as the voltage drop on the resistance) can be written as:

$$\hat{v}_{r,pad} = \sqrt{\left(\frac{4}{\pi}\hat{v}_i\right)^2 + \left(\frac{\hat{i}_r}{\omega C_r}\right)^2} = \sqrt{\left(\hat{v}_r - R_r\hat{i}_r\right)^2 + \left(\omega L_r \hat{i}_r\right)^2} = 1505 \text{ V} \tag{8}$$

This voltage value is useful for the choice of the insulation of the receiving pad.

The electrical scheme of the transmitter section and its equivalent circuit are shown in Figures 11 and 12, respectively. These figures again define the symbols used in the following equations.

In Figure 11 the box labelled "TX PAD" represents the two pads when the receiver is connected to the load. The three-levels, H-bridge inverter is represented in Figure 12 as a voltage generator with a sinusoidal waveform representing the fundamental of the square wave.

The LCL compensation network on the transmitter side is characterized by an auxiliary inductor $L_a = L_t$, while the capacitor has to resonate at the operating frequency with the inductors [30,31]:

$$C_t = \frac{1}{\omega^2 L_t} = 70 \text{ nF} \tag{9}$$

$\overline{Z}_{p,t}$ represents the reflected impedance from the receiving pad to the sending pad:

$$\overline{Z}_{p,t} = R_{p,t} = \frac{\omega^2 M^2}{R_p} = 47.0 \ \Omega \tag{10}$$

If we neglect the parasitic resistance and all the losses in the transmitting pad, the equivalent impedance seen at the inverter terminals is:

$$\overline{Z}_i = \frac{\omega^2 \, L_t^2}{\overline{Z}_{p,t}} = 15.2 \ \Omega \tag{11}$$

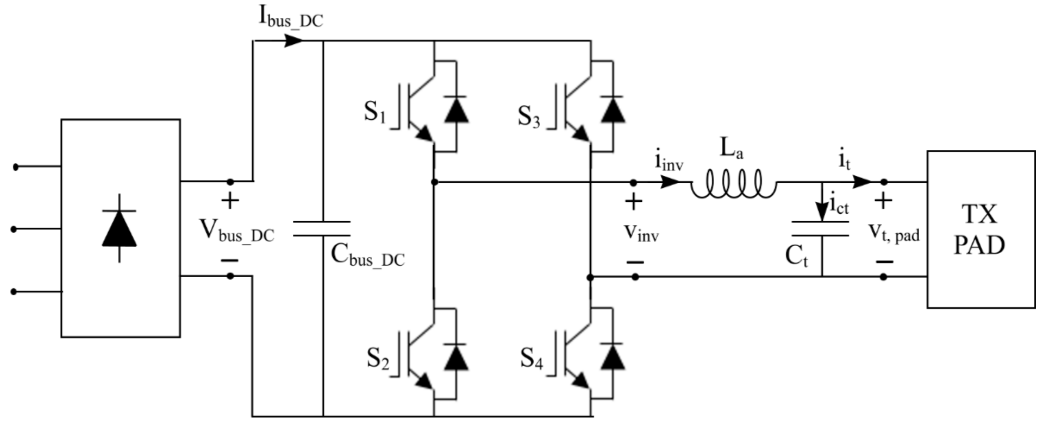

Figure 11. Electrical scheme of the transmitting section. The inverter is a "classical" H bridge, three levels, while the rectified is three-phases bridge one.

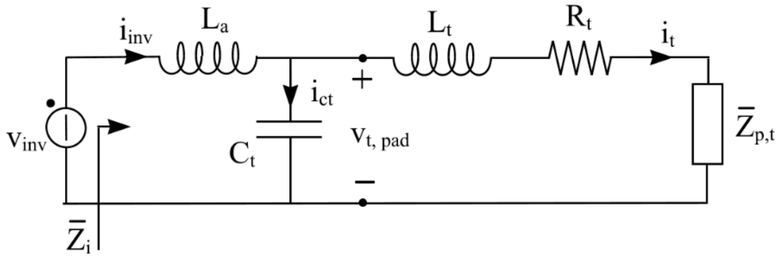

Figure 12. Equivalent circuit of the transmitter section. The feeding inverter is represented by an ideal sinusoidal voltage generator (the fundamental of the generated waveform), the impedance $\overline{Z}_{p,t}$ represents the equivalent impedance of the receiving circuit referred to the transmitting one.

Since this impedance is a pure resistance, the fundamentals of the voltage and of the current on the inverter are in phase. The current on the transmitting pad is obtained by the current divider rule:

$$\dot{I}_t = \frac{\dot{V}_{inv}}{\overline{Z}_i} \frac{\frac{1}{j\omega C_t}}{\frac{1}{j\omega C_t} + j\omega L_t + \overline{Z}_{p,t}} \tag{12}$$

Considering the resonant condition yields:

$$\dot{I}_t = \frac{\dot{V}_{inv}}{j\omega L_t} \tag{13}$$

As known, because of the LCL primary compensation, the current in the transmitting coil does not depend on the load. The peak value of the fundamental of the voltage induced on the receiving pad by the current on the transmitting pad only is expressed as (Figure 10):

$$\hat{v}_r = \omega M \hat{i}_t \tag{14}$$

and consequently:

$$\hat{v}_r = \frac{M}{L_t} \hat{v}_{inv} \tag{15}$$

Neglecting the voltage drop on the resistance of the receiving pad we can also write:

$$\hat{v}_r = \frac{M}{L_t} \hat{v}_{inv} \cong \frac{4}{\pi} \hat{v}_i \tag{16}$$

confirming how the LCL primary–LC secondary compensations allow achieving constant (load-independent) voltage output. The peak value of the current on the transmitting pad correspondent to $\hat{v}_r = 137.5$ V is:

$$\hat{i}_t = \frac{\hat{v}_r}{\omega M} = 12.8 \text{ A} \tag{17}$$

while the peak value of the fundamental of the voltage at the inverter terminals is:

$$\hat{v}_{inv} = \omega L_t \hat{i}_t = 341 \text{ V} \tag{18}$$

The value of the current on the transmitting pad is low enough to ensure the linear behavior of the ferrite cores, thus confirming the hypotheses assumed in Section 4.

The inverter is fed by a three phases bridge rectifier with the output voltage $V_{bus\_DC} = 565$ V, and the phase-shift modulation is adopted. The phase-shift angle correspondent to the square wave whose fundamental has a peak value $\hat{v}_{inv}$ is:

$$\theta = 2 * sin^{-1}\left(\frac{\pi \hat{v}_{inv}}{4 * V_{bus\_DC}}\right) = 0.99 \text{ rad} \tag{19}$$

We can now evaluate voltages and currents on the components to properly size them. The peak current of the current on the inverter is:

$$\hat{i}_{inv} = \frac{\hat{v}_{inv}}{|\overline{Z}_i|} = 23 \text{ A} \tag{20}$$

Considering the other components, the peak value of the voltage on the compensating inductor L_a is $\hat{v}_{L_a} = \omega L_a \hat{i}_{inv} = 615$ V, while the voltage at the terminals of the transmitting pad is:

$$\hat{v}_{t,pad} = \sqrt{\left(R_{p,t}\hat{i}_t + R_B \hat{i}_t\right)^2 + \left(\omega L_t \hat{i}_t\right)^2} = 692 \text{ V} \tag{21}$$

This is also the voltage at the terminals of the capacitor, then the peak value of the fundamental component of the current on the capacitor is:

$$\hat{i}_{C_t} = \omega C_t \hat{v}_t = 26 \text{ A} \tag{22}$$

As far the design of the three-phases bridge rectifier, its rated power can be obtained by considering the power delivered to the rectifier on the receiving side taking into account the efficiency of the devices and components between the two rectifiers. In particular, assuming an efficiency $\eta_{inv} = 0.98$ for the inverter and $\eta_{ipt} = 0.9$ for the two pads including also the losses on the parasitic resistances of the components of the compensation networks.

$$P_{DC\_inv} = \frac{\frac{4}{\pi}\hat{v}_i \hat{i}_r}{2\eta_{ipt}\eta_{inv}} = 4.21 \text{ kW} \tag{23}$$

Considering that $V_{bus\_DC} = 565$ V, the nominal current of the diodes has to be no less than $I_{bus\_DC} = 7.5$ A.

As shown in Figure 11, a capacitor is used to reduce the ripple on the voltage produced by the rectifier bridge; imposing a maximum ripple of 1.7% (i.e., $\Delta V = 9.6$ V), the required capacitance is:

$$C_{bus\_DC} \geq \frac{I_{bus\_DC}}{6f\Delta V} = \frac{7.5}{6 \cdot 50 \cdot 9.6} = 2.6 \text{ mF} \tag{24}$$

The capacitive filter was obtained by parallel connecting of three series connection of two capacitors with $C_1 = 1.8$ mF and $V_{nom} = 500$ V, so obtaining a resultant capacitance of 2.7 mF with a maximum voltage $V_{max} = 1000$ V.

6. Simulation and Experimental Analysis

The performance of the proposed IPT charging system was validated through several simulations and experimental tests. The numerical model of the system was developed in MATLAB-Simulink® environment and a full-scale prototype of the proposed IPT system was designed and implemented.

The power conversion units of the IPT system were dimensioned according to the voltage and current amplitudes calculated in the previous section, which were verified by means of numerical analysis.

In detail, starting from the supply voltage of the IPT system, the three-phase diode bridge SEMIKRON SKD30/14A1 ($V_{max} = 1400$ V, $I_{max} = 30$ A) was adopted for implementing the first stage of the power conversion process.

The H-bridge inverter, connected to the DC-link of the uncontrolled rectifier power unit, is composed by a power board with a superimposed driver board. This solution allows for the optimization the PCB layout of the inverter power section in terms of the reduction of the parasitic elements, which can lead to a switching ringing issue that, as is well-known, determines efficiency loss and possible failure of the power switches.

SiC MOSFET SCTWA50N120, manufactured by STMicroelectronics, was selected as power switch for the inverter power stage. The driver board is based on the STMicroelectronics STGAP2S galvanically isolated single gate driver. Moreover, the inverter power stage is protected by a DC-link overcurrent protection that is based on shunt resistor solution. The voltage across the shunt resistor is compared with a selected threshold voltage by means of an analog voltage comparator, in order to implement a fast current protection.

The output of the voltage comparator is latched through a D-type flip-flop and its output signal is used to disable the gate command coming from the inverter control unit. This unit is based on the Texas Instruments DSP TMS320F28335 that implement the control algorithms of the inverter and determine its gate commands, which are sent to the driver board by means of an optic fiber connection.

As explained in the previous section, the inverter is connected to the transmitter pad by means of a LC network that, resonating with the self-inductance of the transmitting pad, realizes an LCL compensation. The capacitor was implemented by TDK B32672L8103J device in 2S14P configuration for meeting the required value of capacitance, and the voltage and current solicitations of the IPT system as well.

The high frequency rectifier (HFC) and the step-down DC/DC converter of the IPT receiver section were implemented by a single board in order to meet the space constraint of the slave unit. Ultra-fast diode IXYS DSEI 60-02A and INFINEON MOSFET IPB107N20N3GATMA1 with On Semiconductor diode MBRB40250TG were used for implementing the HFC and DC/DC converter, respectively. In detail, the DC/DC converter is based on 5 legs connected in parallel and controlled in interleaved operation. The capacitor of the compensation network of the receiver section was realized by means of TDK B32672L8103J device in 2S14P configuration as for the transmitter section. The control and the modulation algorithm of the DC/DC converter were implemented by means of a dedicated control unit based on Texas Instruments DSP TMS320F28335. The overall layout of the IPT system is shown in Figure 13.

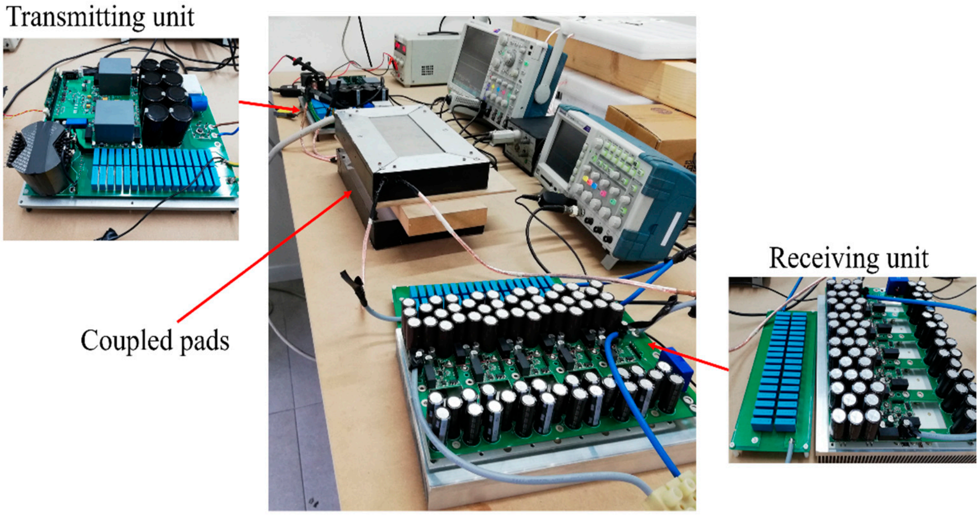

Figure 13. Picture of the layout of the IPT system during the experimental test. The three main components of the system, namely the transmitting unit (rectifier + inverter + compensating networks), the couple pads and the receiving unit (compensating network + rectifier + DC/DC converter) are shown in the insets.

To validate the performance in terms of the power coupling between transmitter and receiver sections of the IPT prototype, experimental tests have been carried out considering an electronic load CHROMA 63,804 instead of the battery pack.

Figures 14 and 15 show the comparison between the numerical and experimental results when the power delivered to the load from IPT system is equal to 3.5 kW with an airgap between the windings of the pads equal to 6 cm.

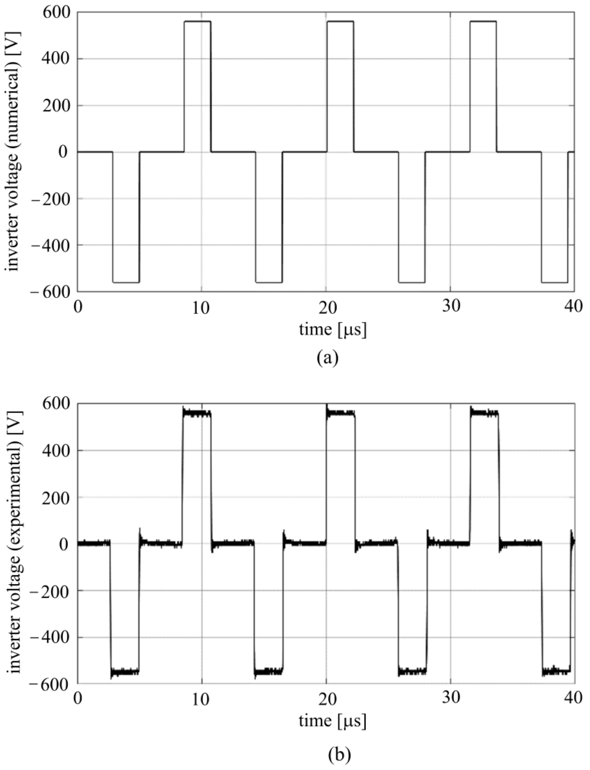

(a)

(b)

Figure 14. Output inverter voltage when a power load equal to a 3.5 kW is requested to IPT system: (**a**) numerical result; (**b**) experimental result.

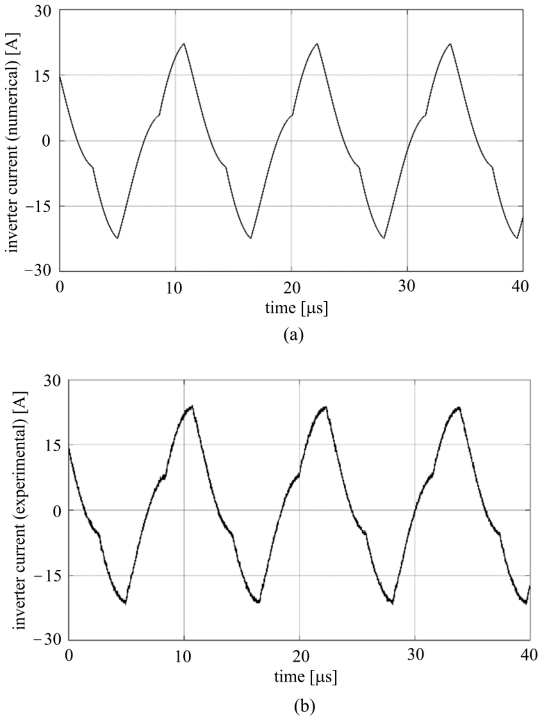

(a)

(b)

Figure 15. Output inverter current when a power load equal to a 3.5 kW is requested to IPT system: (**a**) numerical result; (**b**) experimental result.

Figure 15a,b, respectively, show the output current waveforms of the inverter for the numerical and experimental analysis. A good agreement between numerical and experimental results is achieved in terms of the current as well. This allows validating the proposed design and performance of the IPT system.

Finally, Figure 16 reports the measured time waveform of the instantaneous power entering the DC/DC converter. In this case again, the measured quantity is in excellent agreement with the predicted one.

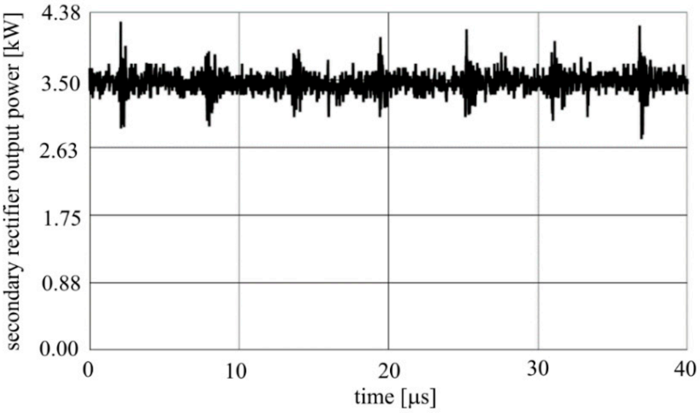

Figure 16. Measured output secondary rectifier power in nominal conditions. The surges in the waveform of the power from the secondary rectifier are caused by the switch ringing and are more evident in correspondence to the instants when the conduction of the MOSFETS begin.

7. Discussion

This section is devoted to finalizing the discussion about some aspects previously presented in the paper. The main issues are related to the change of the adopted energy storage system and to the introduction of the IPT in terms of safety issues and a better management of the battery charging. The design procedure deserves a short comment too.

The substitution of the original storage system based on a supercapacitor plus an LFP battery with a Ni–MH battery allowed an important saving of space and weight, especially on the slave shuttle. This space was used to accommodate the receiving section (pad and power electronics) of the IPT system. As previously observed in the paper, IPT charging is able to fully exploit the time when the slave is parked on the master for charging the battery pack. Since IPT systems are intrinsically free of sparks, the charging process can start as soon as the slave reach the master. Looking at Figure 2 we can see that in the original system the power transfer takes place during only half of the time interval labelled with “charge”. By using the IPT system the charging time is nearly doubled and the same energy can be delivered to the slave with a reduced (substantially halved) power level. Another valuable outcome of the absence of sparks is the possibility of extending the use of the system to warehouses where potentially explosive atmospheres may be present. This would allow the project leader to expand the range of products available on the market.

Finally, as so far discussed in the paper, the sizing of each unit (power electronics, transmitting and receiving pads, compensating networks) is tightly related to the design of the other ones. The integrated approach adopted in this paper has proven to be able to manage these relations.

8. Conclusions

In this paper we discussed in detail the design of a system for IPT used for the battery charge of shuttles in automated warehouses. All the components that constituted the system were sized on purpose taking into account the constraints imposed by the pre-existing mechanical layout and by the working profile of the shuttle. Several design tools were adopted for the design of the components (FEM analysis for the pads, circuital CAD for the PCB and power electronics) as well as for the numerical modeling of the whole system (MATLAB-Simulink® environment).

A prototype was built according to the design and a measurement campaign was performed. The results of the simulations are in excellent agreement with the experimental data.

Author Contributions: Conceptualization, A.M., R.R. and G.T.; methodology, M.C. and R.R.; software, G.L., V.C. and M.D.M.; validation, G.T., M.D.M. and V.C.; investigation, G.T.; data curation, M.C.; writing—original draft preparation, A.M., G.L. and M.D.M.; writing—review and editing, R.R. and V.C.; supervision, A.M.; funding acquisition, M.C. All authors have read and agreed to the published version of the manuscript.

Funding: This research was funded by the Toscana Region in the framework of MAG-IA project, grant number POR FESR 2014-2020, CUP 7165.24052017.112000040.

Data Availability Statement: All the relevant data is contained in the article.

Conflicts of Interest: The authors declare no conflict of interest.

References

1. MAG-IA Project. Available online: https://www.destec.unipi.it/ricerca/progetti-nazionali-ed-internazionali/por-creo (accessed on 30 June 2021).
2. Cassioli Group Magazzini Automatici Official Site. Available online: https://www.cassioli.it (accessed on 30 June 2021).
3. Ceraolo, M.; Lutzemberger, G.; Poli, D.; Scarpelli, C.; Sabatini, M. Experimental analysis of Ni-MH high power cells. In Proceedings of the UPEC 2020—55th International Universities Power Engineering Conference, Turin, Italy, 1–4 September 2020.
4. Tudoroiu, N.; Elefterie, L.; Burdescu, D.; Tudoroiu, E.R.; Kecs, W.; Dobritoiu, M.; Ilias, N.; Casavela, V.S. On-board real-time state-of-charge estimators of hybrid electric vehicles Ni-MH battery. In Proceedings of the 8th International Conference ICITEE, Yogyakarta, Indonesia, 5–6 October 2016; pp. 1–6.
5. Hafeez, A.; Alghodhaifi, H.; Sadeq, T. State of charge estimation and state space model analysis of the Ni-MH battery system. In Proceedings of the 2017 IEEE Conference on Energy Conversion (CENCON), Kuala Lumpur, Malaysia, 30–31 October 2017; pp. 61–66.
6. Muhsen, H.; Al-Muhtady, A.; Kadri, A.; Ruziyeh, A. Evaluating and Repurposing of Used Ni-MH Hybrid Batteries. In Proceedings of the 2017 International Renewable and Sustainable Energy Conference (IRSEC), Tangier, Morocco, 4–7 December 2017; pp. 1–5.
7. Wei, X.; Wang, Z.; Dai, H. A Critical Review of Wireless Power Transfer via Strongly Coupled Magnetic Resonances. *Energies* **2014**, *7*, 4316–4341. [CrossRef]
8. Trivino, A.; Gonzalez-Gonzalez, J.M.; Aguado, J. A Wireless Power Transfer Technologies Applied to Electric Vehicles: A Review. *Energies* **2021**, *14*, 1547. [CrossRef]
9. Sarrazin, B.; Derbey, A.; Albouy, P.; Ferrieux, J.P.; Meunier, G.; Schanen, J.L. Bidirectional wireless power transfer system with wireless control for electrical vehicle. In Proceedings of the 2019 IEEE Applied Power Electronics Conference and Exposition (APEC), Anaheim, CA, USA, 17–21 March 2019.
10. Jiang, J.; Bao, Y.; Wang, L.Y. Topology of a Bidirectional Converter for Energy Interaction between Electric Vehicles and the Grid. *Energies* **2014**, *7*, 4858–4894. [CrossRef]
11. Kim, D.; Abu-Siada, A.; Sutinjo, A. State-of-the-art literature review of WPT: Current limitations and solutions on IPT. *Electr. Power Syst. Res.* **2018**, *154*, 493–502. [CrossRef]
12. Kim, D.; Abu-Siada, A.; Sutinjo, A. A Novel Application of Frequency Response Analysis for Wireless Power Transfer System. In Proceedings of the 2017 IEEE Australasian Universities Power Engineering Conference (AUPEC), Melbourne, Australia, 19–22 November 2017.
13. Baroi, S.; Islam, M.S.; Baroi, S. Design and Simulation of a Wireless Charging System for Electric Vehicles. In Proceedings of the 2nd International Conference on Electrical & Electronic Engineering (ICEEE), Rajshahi, Bangladesh, 27–29 December 2017.
14. Wang, P.; Sun, Y.; Li, Z.; Ye, Z. An Optimization Method for Simultaneous Wireless Power and Data Transfer Systems. *Electronics* **2020**, *9*, 2073. [CrossRef]
15. Barmada, S.; Tucci, M.; Fontana, N.; Dghais, W.; Raugi, M. Design and Realization of a Multiple Access Wireless Power Transfer System for Optimal Power Line Communication Data Transfer. *Energies* **2019**, *12*, 988. [CrossRef]
16. Barmada, S.; Dionigi, M.; Mezzanotte, P.; Tucci, M. Design and experimental characterization of a combined WPT–PLC system. *Wirel. Power Transf.* **2017**, *4*, 160–170. [CrossRef]
17. Pellitteri, F.; Campagna, N.; Castiglia, V.; Damiano, A.; Miceli, R. Design, implementation and experimental results of an inductive power transfer system for electric bicycle wireless charging. IET Renewable Power Generation. *IET Renew. Power Gener.* **2020**, *14*, 2908–2915. [CrossRef]
18. Liu, Z.; Li, F.; Tao, C.; Li, S.; Wang, L. Design of wireless power transfer system for autonomous underwater vehicles considering seawater eddy current loss. *Microsyst. Technol.* **2021**, *27*, 3783–3792. [CrossRef]

19. Lee, C.H.; Jung, G.; Al Hosani, K.; Song, B.; Seo, D.K.; Cho, D. Wireless Power Transfer System for an Autonomous Electric Vehicle. In Proceedings of the 2020 IEEE Wireless Power Transfer Conference (WPTC), Seoul, Korea, 15–19 November 2020.
20. Arts Energy Official Site. Available online: https://www.arts-energy.com/solutions-en/ni-mh-battery-pack/specifications-of-use-mh (accessed on 30 March 2020).
21. Fritzson, P. *Introduction to Modeling and Simulation of Technical and Physical Systems with Modelica*; Wiley-IEEE Press: Hoboken, NJ, USA, 2011.
22. Ceraolo, M.; Lutzemberger, G.; Mati, R.; Sani, L. Realisation and test of a fuel-cell based vehicle. In Proceedings of the ENERGYCON 2012 IEEE International Conference, Florence, Italy, 9–12 September 2012.
23. Ceraolo, M.; Giglioli, R.; Lutzemberger, G.; Sani, L. Hybrid energy systems in mobility applications. In Proceedings of the 2016 AEIT Interna-tional Annual Conference (AEIT), Capri, Italy, 5–7 October 2016.
24. Ceraolo, M.; Lutzemberger, G.; Doveri, N. Experiences of realisation and test of a fuel-cell based vehicle. In Proceedings of the SPEEDAM 2010, International Symposium on Power Electronics, Electrical Drives, Automation and Motion, Pisa, Italy, 14–16 June 2010.
25. Ecker, M.; Nieto, N.; Käbitz, S.; Schmalstieg, J.; Blanke, H.; Warnecke, A.; Sauer, D.U. Calendar and cycle life study of Li(NiMnCo)O2-based 18650 lithium-ion batteries. *J. Power Sources* **2014**, *248*, 839–851. [CrossRef]
26. Park, J.; Appiah, W.A.; Byun, S.; Jin, D.; Ryou, M.H.; Lee, Y.M. Semi-empirical long-term cycle life model coupled with an electrolyte depletion function for large-format graphite/LiFePO4 lithium-ion batteries. *J. Power Sources* **2017**, *365*, 257–265. [CrossRef]
27. Maxwell Technologies Official Site. Available online: https://www.maxwell.com/products/ultracapacitors/cells (accessed on 30 March 2020).
28. Kalwar, K.A.; Mekhilef, S.; Seyedmahmoudian, M.; Horan, B. Coil Design for High Misalignment Tolerant Inductive Power Transfer System for EV Charging. *Energies* **2016**, *9*, 937. [CrossRef]
29. Bi, Z.; Kan, T.; Mi, C.C.; Zhang, Y.; Zhao, Z.; Keoleian, G.A. A review of wireless power transfer for electric vehicles: Prospects to enhance sustainable mobility. *Appl. Energy* **2016**, *179*, 413–425. [CrossRef]
30. Zhang, W.; Mi, C.C. Compensation topologies for High-Power Wireless Power Transfer Systems. *IEEE Trans. Veh. Technol.* **2016**, *65*, 4768–4778. [CrossRef]
31. Chen, Y.; Zhang, H.; Park, S.; Kim, D. A Comparative Study of S-S and LCCL-S Compensation Topologies in Inductive Power Transfer Systems for Electric Vehicles. *Energies* **2019**, *12*, 1913. [CrossRef]
32. Available online: http://www.elettrofili.it/litz_wires.html (accessed on 6 July 2021).
33. Yang, Y.; Cui, J.; Cui, X. Design and Analysis of Magnetic Coils for Optimizing the Coupling Coefficient in an Electric Vehicle Wireless Power Transfer System. *Energies* **2020**, *13*, 4143. [CrossRef]
34. Budhia, M.; Boys, J.T.; Covic, G.A.; Huang, C.-Y. Development of a single-sided flux magnetic coupler for electric vehicle IPT charging systems. *IEEE Trans. Ind. Electron.* **2013**, *60*, 318–328. [CrossRef]
35. Siferrit Material N87, EPCOS AG 2017. Available online: https://www.tdk-electronics.tdk.com (accessed on 25 August 2021).
36. Musolino, A.; Rizzo, R.; Tripodi, E.; Toni, M. Modeling of electromechanical devices by GPU-accelerated integral formulation. *Int. J. Numer. Model. Electron. Netw. Devices Fields* **2013**, *26*, 376–396. [CrossRef]
37. Tripodi, E.; Musolino, A.; Rizzo, R.; Raugi, M. A new predictor–corrector approach for the numerical integration of coupled electromechanical equations. *Int. J. Numer. Methods Eng.* **2016**, *105*, 261–285. [CrossRef]
38. EFFE. *User Manual 2009*; Bathwick Electrical Design Ltd.: Bath, UK, 2009.
39. Barmada, S.; Fontana, N.; Sani, L.; Thomopulos, D.; Tucci, M. Deep learning and reduced models for fast optimization in electromagnetics. *IEEE Trans. Magn.* **2020**, *56*, 1–4. [CrossRef]
40. Bertoluzzo, M.; Di Monaco, M.; Buja, G.; Tomasso, G.; Genovese, A. Comprehensive development of dynamic wireless power transfer system for electric vehicle. *Electronics* **2020**, *9*, 1045. Available online: https://www.mdpi.com/2079-9292/9/6/1045 (accessed on 25 August 2021). [CrossRef]